Band gap formation and Anderson localization in disordered photonic materials with structural correlations

Luis S. Froufe-Pérez[a], Michael Engel[b], Juan José Sáenz[c,d], and Frank Scheffold[a,1]

[a]Department of Physics, University of Fribourg, CH-1700 Fribourg, Switzerland; [b]Institute for Multiscale Simulation, Friedrich-Alexander University Erlangen-Nürnberg, 91052 Erlangen, Germany; [c]Donostia International Physics Center, 20018 Donostia-San Sebastián, Spain; and [d]Ikerbasque, Basque Foundation for Science, 48013 Bilbao, Spain

Disordered dielectric materials with structural correlations show unconventional optical behavior: They can be transparent to long-wavelength radiation, while at the same time have isotropic band gaps in another frequency range. This phenomenon raises fundamental questions concerning photon transport through disordered media. While optical transparency in these materials is robust against recurrent multiple scattering, little is known about other transport regimes like diffusive multiple scattering or Anderson localization. Here, we investigate band gaps, and we report Anderson localization in 2D disordered dielectric structures using numerical simulations of the density of states and optical transport statistics. The disordered structures are designed with different levels of positional correlation encoded by the degree of stealthiness χ. To establish a unified view, we propose a correlation-frequency (χ–ν) transport phase diagram. Our results show that, depending only on χ, a dielectric material can transition from localization behavior to a band gap crossing an intermediate regime dominated by tunneling between weakly coupled states.

disordered photonics | photonic band gap materials | Anderson localization of light | mesoscopic wave transport | hyperuniform structures

Light propagation through a dielectric medium is determined by the spatial distribution of the material. Photons scatter at local variations of the refractive index. For a periodically organized system, interference dominates light transport and is responsible for optical phenomena in opal gems and photonic crystals (1). In random media, transport becomes diffusive through successive scattering events. The characteristic length scale over which isotropic diffusion takes place is the transport mean free path. Materials thicker than the mean free path appear cloudy or white. However, when scattering centers are locally correlated, diffraction effects can be significant. The description of light transport then becomes a challenging problem with many applications, such as the transparency of the cornea to visible light (2), the strong wavelength dependence of the optical thickness of colloidal suspensions (3) and amorphous photonic structures (4, 5), and structural colors in biology (6). Critical opalescence and the relatively large electrical conductivity of disordered liquid metals (7) are closely related phenomena.

In the weak scattering limit, photon transport is diffusive and can be described by a local collective scattering approximation, which states that the mean free path $l_t = (\rho \sigma_t)^{-1}$ is inversely proportional to the number density of scatterers ρ and to the effective transport cross-section (7–9)

$$\sigma_t = \int \frac{d\sigma}{d\Omega} S(k_\vartheta)(1 - \cos \vartheta) d\Omega. \qquad [1]$$

Here, $d\sigma/d\Omega$ is the differential cross-section for an isolated scatterer and $k_\vartheta = 2k \sin(\vartheta/2)$ is the momentum transfer. This equation relates positional correlations of the optical medium to

transport via the structure factor $S(k_\vartheta)$. In the past, the local collective scattering approximation has been applied to dense and strongly scattering media (9), but the validity of this approach is limited, as it does not include near-field corrections and recurrent scattering (10, 11). Clearly, the recently discovered isotropic band gaps (12, 13) in hyperuniform disordered photonic materials (HDPMs) cannot be derived from Eq. **1**.

For quasi-one-dimensional (Q1D; waveguides) and 2D uncorrelated or fully random media with $S(k_\vartheta) \equiv 1$, the optical transport properties are well understood. According to the single parameter scaling (SPS) hypothesis (14, 15), statistical properties of transport are governed by a single parameter that can be expressed as the ratio of a characteristic (localization) length ξ to system size L. While for $L/\xi \ll 1$ transport is diffusive, SPS predicts a cross-over to the Anderson localization regime $L/\xi \gg 1$.

The opposite limit of a periodically repeating structure, a photonic crystal with sharp Bragg peaks in the structure factor and a full band gap in three dimensions, was discussed in the late 1980s in the pioneering works of Yablonovitch and John (16, 17). As pointed out by John at that time, perturbative introduction of disorder in a crystal can induce strongly localized states in the photonic band gap (PBG), leading to a pseudogap in the photon density of states (DOS), in analogy with electronic pseudogaps in amorphous semiconductors. Strong Anderson localization might then be accessible in the pseudogap frequency range, and there

Significance

It has been shown recently that disordered dielectrics can support a photonic band gap in the presence of structural correlations. This finding is surprising, because light transport in disordered media has long been exclusively associated with photon diffusion and Anderson localization. Currently, there exists no picture that may allow the classification of optical transport depending on the structural properties. Here, we make an important step toward solving this fundamental problem. Based on numerical simulations of transport statistics, we identify all relevant regimes in a 2D system composed of silicon rods: transparency, photon diffusion, classical Anderson localization, band gap, and a pseudogap tunneling regime. We summarize our findings in a transport phase diagram that organizes optical transport properties in disordered media.

should be a cross-over between these two transport regimes as the structure factor evolves between the two extreme limits of a structureless random medium and Bragg-peaked shape typical of a full band gap photonic crystal (17). However, 30 years after John's proposal, an experimental realization or a theoretical description of the statistical properties of photon transport in the cross-over regime from weakly to strongly correlated disordered media remains poorly understood, both in three and two dimensions.

For correlated but fully disordered media, a situation clearly distinct from disordered crystals, attention over the last years focused on the emergence of unexpected optical properties like optical transparency (18, 19) and PBGs in 2D and 3D high-refractive-index disordered materials (12, 13, 20, 21). In particular, the concept of stealthy hyperuniformity as a measure for the hidden order in amorphous materials has drawn significant attention (18, 22, 23). HDPMs are disordered, but uniform without specific defects, and the DOS can be strictly zero. A key parameter controlling structural correlations of HDPM, and thus the band-gap width, is the degree of stealthiness χ, defined as the ratio between the number of constrained degrees of freedom to the total number of degrees of freedom (18). It is currently not known what effect χ has on the statistics of wave transport in HDPM outside the gap and whether the transport properties in HDPM can be understood in terms of SPS. Neither is anything known about the transport properties for frequencies ν near the band edge, a regime where disordered crystalline materials exhibit a rich and complex transition toward Anderson localization (24).

At the same time, experimental observations of Anderson localization of light have been questioned repeatedly, particularly in 3D systems (25, 26). The current state of the debate is that Anderson localization of light is absent in 3D fully random media (27) and thus can only be reached in the presence of correlations (26). However, correlated disordered media have also been shown to possess full band gaps for materials with similar optical contrast previously associated to Anderson localization (28, 29), both in two and three dimensions (12, 21). Currently, there exists no picture that may allow one to predict or classify the different optical transport regimes in disordered photonic materials with structural correlations. The main goal of our work is to address these fundamental questions and to propose a correlation–frequency (χ–ν) phase diagram for wave transport through disordered dielectric media.

Results and Discussion

Transport Phase Diagram. A relatively simple example of a correlated disordered medium is a collection of infinite parallel cylinders of high-refractive index that are distributed according to a 2D stealthy hyperuniform (SHU) point pattern (Fig. 1, *Insets*) (18, 22, 23). The area of the pattern $A = L \times L$ and the number of points N define a characteristic length a through the number density $\rho = N/A \equiv a^{-2}$. When the electric field is parallel to the cylinder axes (TM polarization), the propagation of light with a wave vector perpendicular to the axes can be described by a 2D Schrödinger-like scalar equation with identical scatterers. This setup provides an ideal laboratory to explore the statistical properties of wave transport in 2D HDPM. The normalized DOS (NDOS) as a function of frequency for a 2D SHU pattern of monodisperse high-refractive index cylinders has been reported for different values of χ (12, 13).

Based on the NDOS and the results for 2D disordered crystals (30, 31), we first make a hypothesis about the transport phase diagram of 2D HDPM in Fig. 1. For strongly correlated, nearly crystalline materials (high χ), stealth (transparent) and gap intervals are adjacent to each other, reminiscent of the conduction band and stop gap for electrons and photons in crystals. Lowering the degree of stealthiness to $\chi < 0.5$, the gap and stealth
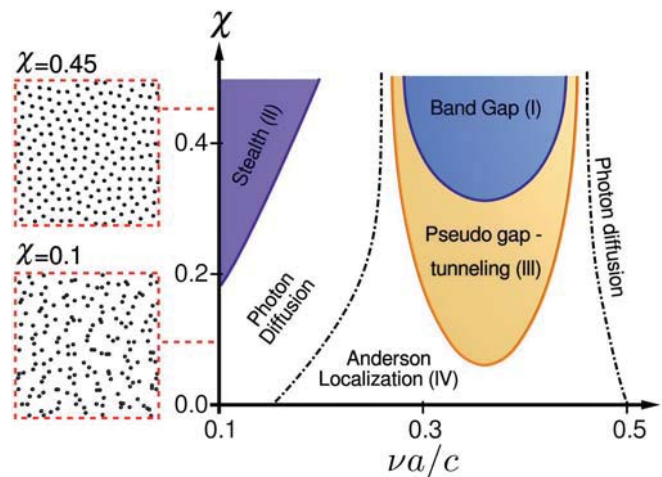
Fig. 1. Correlation-frequency (χ–ν) transport phase diagram for HDPMs. A box of size $L \times L$ is filled with high-refractive index ($\varepsilon = 11.6$) cylinders distributed according to a 2D stealthy hyperuniform (SHU) point pattern. The cylinder radius is $0.189a$, and the filling fraction is 11.2% (13). The degree of stealthiness is denoted χ (18). ν is the optical frequency, c the vacuum speed of light, and a is the mean distance between scatterers. In the central region (*I*), a wide photonic gap opens, inhibiting the propagation of transverse-magnetic (TM) polarized electromagnetic waves (12, 13). In this region, the DOS is exactly zero, and evanescent light waves decay exponentially over distances shorter than the characteristic structural length scale $\xi < a$. In the stealth region (*II*), on the left side of the band gap, the material is transparent. In the vicinity of the gap, for smaller values of χ, the DOS is suppressed but nonzero (*III*), and evanescent waves can tunnel between isolated states with a decay length $\xi \sim a$. Sufficiently far from the gap, diffuse light transport may cross over to strong Anderson localization. The transition from diffusive to localized transport (dotted line) is system size-dependent, and we expect that SPS–Anderson localization (*IV*) in the limit of sample sizes $L > \xi > a$. Eventually, at high χ, we enter the crystal regime (*Isotropy of the SHU Seed Patterns* and Fig. S1) (12, 13).

intervals shrink. In the newly accessible intervals in between the stealth and the gap regions, the material possesses a reduced DOS and displays significant scattering. We expect a tunneling regime (non-SPS) for frequencies near the band gap and a diffusive scattering regime further apart. The tunneling regime is intimately related to the pseudogap in which the DOS is low, but finite. Once the DOS is sufficiently high, far away from the gap, diffusive transport sets in and a cross-over to classical Anderson localization (SPS) should occur as $L > \xi$. For high frequencies, we also expect diffusive transport, independent of χ, since in this spectral region, the scattering strength decays below the threshold where a gap opens.

Numerical Simulations. Although the calculation of the standard transport mean free path can be useful to describe transport processes in disordered correlated media in frequency ranges where the system is almost transparent or transport is diffusive (9, 19), it loses its meaning in a region where the DOS is zero. Identifying the different transport regimes requires the numerical solution of the full multiple scattering problem in a wide spectral range. We calculate the decay of the intensity of the wave fields along the propagation direction and the full statistics of wave transport. First, we generate a statistical ensemble of 1,000 patterns of ~ 200 monodisperse high refractive index cylinders for each value of χ as described in ref. 13. Our 2D point patterns show stealthy hyperuniformity, which means that not only long-range density fluctuations are suppressed, $S(k_\vartheta \to 0) = 0$, but the structure factor vanishes over a finite range, $S(k_\vartheta < k_c) = 0$. The critical wave number k_c sets the phase boundary of the stealth phase (13, 19). With these parameters, a PBG opens at a central

frequency $\nu_0 a/c \simeq 0.35$, and the PBG expands to a maximum width of $\Delta\nu/\nu_0 \simeq 45\%$ (13). Following work on disordered crystals (30, 31), we introduce the length

$$\ell_{DOS}(\nu, \chi) = \frac{a}{\sqrt{NDOS(\nu, \chi)}} \qquad [2]$$

as an effective measure of the mean distance between states. Fig. 2A shows a map of a/ℓ_{DOS}. We can clearly identify the gap with no states and infinite ℓ_{DOS} (white region bounded by dashed line) and a pseudogap region where the NDOS is significantly reduced, $\ell_{DOS} \gg a$.

To obtain the characteristic decay length ξ and to sample the statistical properties of transport, we apply the well-known generalized scattering matrix (GSM) method (32) to slabs of thickness $L < L_{max}$ in propagation direction (*GSM Method* and Figs. S2 and S3). Periodic boundary conditions (Fig. 3, *Inset*) define a set of transversal propagation channels. The optical analog g of electrical conductance can be computed from Landauer's formula. If T_{ij} is the intensity transmitted from incoming channel j to outgoing channel i, then the conductance of the system is $g = \sum_{ij} T_{ij}$. The exponential decay length ξ of the conductance is determined by using a fit to $\langle \ln(g(L)) \rangle = -2L/\xi$ (33). Fluctuations are suppressed by performing an ensemble average $\langle \cdot \rangle$ over 1,000 realizations for each frequency and degree of stealthiness. Fig. 2B shows a map of a/ξ. The solid line corresponds to the boundary $\ell_{DOS} = \xi$. Based on studies of 2D disordered crystals (31), we expect this line to indicate the boundary between non-SPS and SPS regions. We repeat the calculations of the DOS and the transport statistics for different systems sizes $N \simeq 100, 310, 480$ and find similar results irrespective of size (*Transport Characteristics*, Table S1, and Figs. S6 and S7).
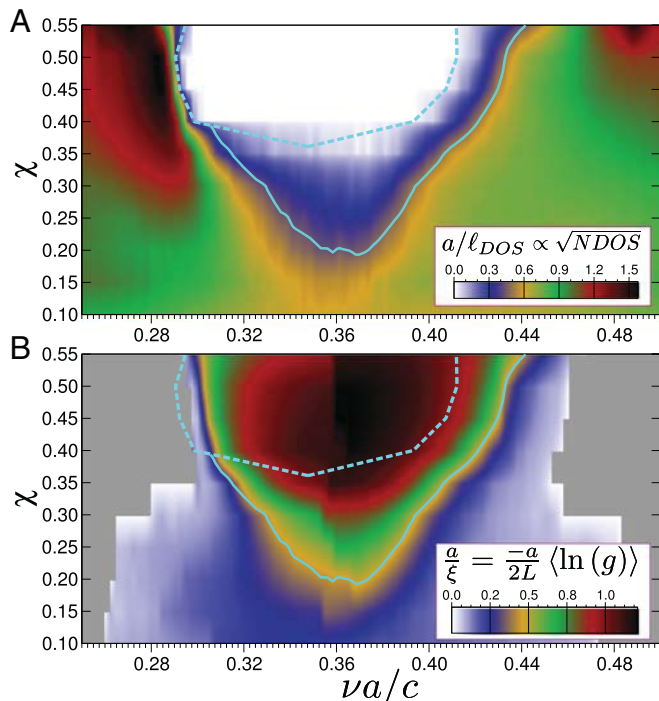
Fig. 2. (A) Ratio of the characteristic length a in the system to the mean distance between states ℓ_{DOS} as a function of frequency $\nu a/c$ and the degree of stealthiness χ for SHU systems. The latter is proportional to the square root of the NDOS. (B) Ratio of a to the decay length ξ. The decay length $\xi = -2L/\langle \ln(g(L)) \rangle$ can only be extracted if the conductance of the system $g \lesssim 1/2$. The other areas are left blank. The dashed line delineates the band gap, and the solid line indicates $\xi = \ell_{DOS}$ in Figs. 2–4.
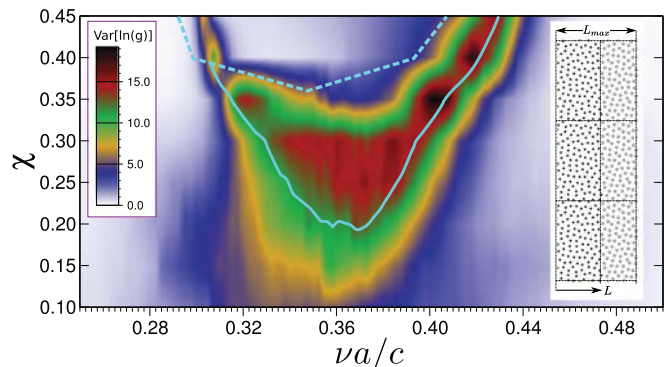
Fig. 3. Fluctuations of the logarithm of the conductance Var(ln(g)) after TM-polarized electromagnetic waves passed through the system, $L = L_{max}$. *Inset* shows the simulation setup of the SHU pattern with dielectric cylinders using periodic boundary conditions in transverse directions.

Transport Fluctuations and Conductance Distribution. So far, we identified regions with exponential decay of the conductance, but did not reveal the physical mechanism responsible for this rapid decay. To this end, we analyze the optical transport statistics (34). Fig. 3 shows a color map of fluctuations in the logarithmic conductance Var(ln(g)) for transmission through the whole system. As expected, regions associated with a PBG do not show substantial fluctuations despite a small decay length ξ signaling transport by direct tunneling through the whole sample. Outside the gap, large fluctuations are most pronounced in the pseudogap regime, $0 < \xi/\ell_{DOS} \lesssim 1$, indicating tunneling-like transport (31). Eventually, further away from the gap, in the regime with $\xi/\ell_{DOS} > 1$, fluctuations decay rapidly.

To discriminate between tunneling-like transport and classical Anderson localization (SPS), we consider the statistical distribution $P(g)$ of the conductance. A quantitative description for transport fluctuations in Q1D systems is given by the Dorokhov–Mello–Pereyra–Kumar (DMPK) equation (35–37). DMPK predicts a cross-over between the diffusive and localized regimes. While $P(g)$ is Gaussian in the diffusive regime, it has a peculiar shape at the onset of the localized regime corresponding to $\langle g \rangle \approx 1/2$ with a marked discontinuity in the first derivative of the distribution and a sharp cutoff beyond $g = 1$ (37, 38). As $\langle g \rangle$ decreases, this cutoff eventually leads to one-sided log-normal distributions for the conductance. Although the DMPK results were derived for the Q1D case, the characteristic shape of $P(g)$ at the onset of the localized regime was exactly reproduced by numerical simulations in 2D disordered systems in the SPS regime (39). We apply a similarity analysis of the numerical $P(g)$ results in our HDPM system and the DMPK result (37) to identify regions where classical Anderson localization (SPS) occurs. A map of the similarity $S(\nu, \chi)$ is shown in Fig. 4. Outside the gap and pseudogap regions, $S > 0.5$ and light transport evolves from diffusion, where the conductance distributions are Gaussian, to Anderson localization, where the distribution is one-side log-normal. The behavior of $P(g)$ in the pseudogap region indicates remarkable differences in the statistical properties, which suggests that SPS is violated in this region.

Conclusions

In conclusion, our numerical results fully support the proposed transport phase diagram in Fig. 1 for 2D photonic structures derived from SHU point patterns. Based on the importance of positional correlations for the appearance of PBGs (13), we expect that other features of the transport phase diagram can also be transferred to disordered point patterns that possess different types of correlated disorder, as long as the patterns
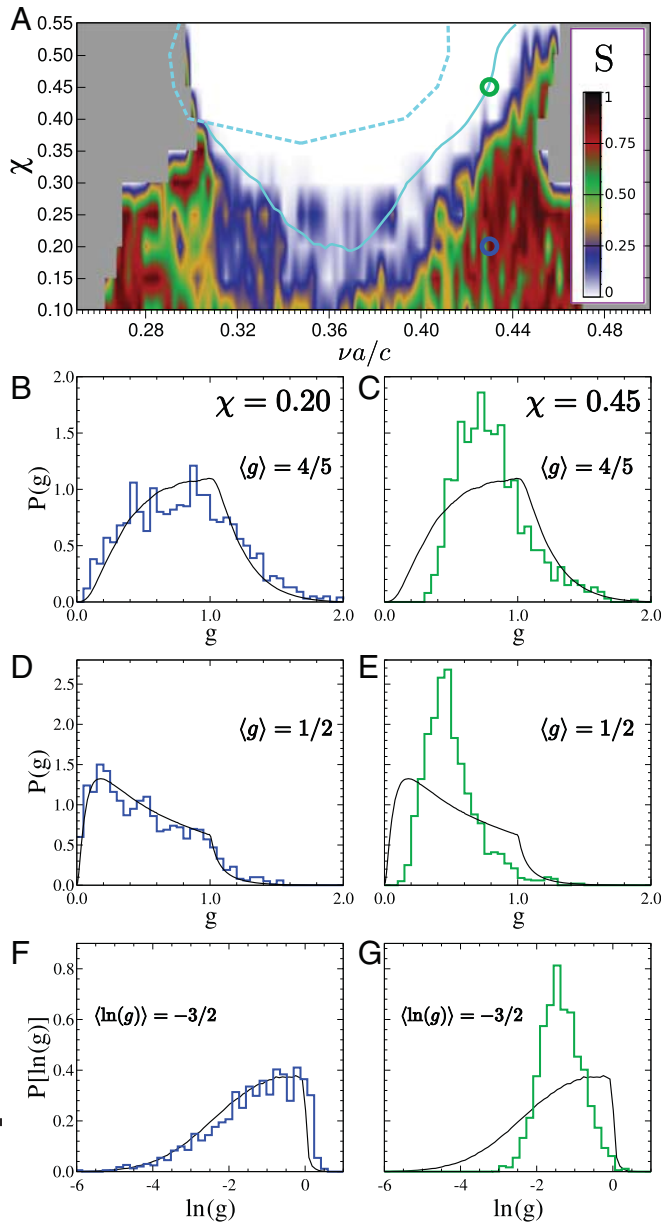
Fig. 4. (A) Similarity map $S(\nu, \chi)$ for the conductance distribution at $\langle g \rangle = 1/2$. High values indicate that the conductance distribution $P(g)$ is similar to the one predicted by Dorokhov–Mello–Pereyra–Kumar (DMPK). The function $S(\nu, \chi)$ is bounded in [0, 1]. (B–G) Conductance distribution for two typical situations, in the SPS regime, $\chi = 0.20$ and in the tunneling regime inside the pseudogap, $\chi = 0.45$. Numerical results are compared with predictions of DMPK (black lines).

become uniform in the large-scale limit—in other words, they are, for example, hyperuniform, nearly hyperuniform (13, 21), or local self-uniform (40). In this case, χ has to be replaced by a measure for the degree of positional correlation. Whether certain details of the positional correlations affect the existence of specific regions in the transport phase diagram and how they move the boundaries delineating the different regions is the subject of follow-up work.

It will be interesting to establish a similar transport phase diagram in three dimensions. In this case, a sharp phase boundary, known as the mobility edge and set by the Ioffe–Regel criterion $kl_t \lesssim 1$ (24, 41), is expected between photon diffusion and Anderson localization (dash-dotted line in Fig. 1).

An important direction for future work is the implications of the phase diagram for electronic transport. It has been argued that SHU plays a role in the formation of electronic band gaps, for example, in amorphous silicon (42). However, the influence of structural correlations and hyperuniformity on electron transport and localization in two or higher dimensions is far from being understood (43).

Methods

Generation of Stealthy Hyperuniform Point Pattern. We use a simulated annealing relaxation scheme to generate disordered SHU patterns with $S(k) < 10^{-6}$ for $k < k_c(\chi)$ as described in our previous work (13). Patterns below the critical parameter $\chi \sim 0.55$, above which quasi-long-range order gradually appears (23), already show significant short-range order. The point patterns are decorated with dielectric cylinders as described in the text.

Band Structure Calculation. We calculate the NDOS using the supercell method (1) implemented in the open-source code MIT Photonic Bands (44). The supercell is repeated periodically, and the band structure is calculated by following the path $\Gamma \to M \to X \to \Gamma$ in reciprocal space. The procedure is described in detail in ref. 13. Nearly identical strategies have also been applied by others (12). We note that, within the spectral range surrounding the band gap region, the results are not affected by the artificial periodicity of the supercell.

GSM Method. We use the improved GSM method. A summary of the method is provided in ref. 32. In the GSM, the system is discretized in slices in the propagation direction. For each slice, the wave equation is solved and the scattering matrix is calculated. By sequentially combining the corresponding scattering matrices, the total scattering matrix of the system up to a length L is obtained.

DMPK Equation. The DMPK equation is a Fokker–Planck equation describing the evolution of coherent wave transport statistics as a function of the ratio of the system length to the transport mean free path. It was shown to describe quantitatively the transport properties of disordered Q1D systems. There is evidence that the DMPK distributions retain the main properties of the conductance distributions in the metallic, critical, and localized regime also in higher dimensions (15, 38). The DMPK distributions were obtained as described in ref. 45 (*DMPK Equation* and Figs. S4 and S5).

Similarity Analysis. The similarity between the conductance distributions of correlated systems and the ideal DMPK distribution is characterized by a similarity function. We first create numerically a finite sample of DMPK conductance histograms with a certain bin size. We quantify differences between the ideal DMPK sample and the results obtained by the GSM by calculating a squared distance distribution function $P(D^2)$. The squared distance between two distributions $P_i(g)$ and $P_j(g)$ is given by

$$D_{i,j}^2 \equiv \int dg \, [P_i(g) - P_j(g)]^2. \qquad [3]$$

In other contexts, the squared distance D^2 is denoted χ^2 or chi-squared. We do not make use of this notation to avoid confusion with the degree of stealthiness χ. For a set of different, but otherwise statistically equivalent, finite-sampling distributions $P_i(g)$, we can define the distribution of squared distances $P(D^2)$ considering all distances $D_{i,j}$ corresponding to all pairs with $i \neq j$. To assess the similarity between $P(D^2)$ and the reference $P_{DMPK}(D^2)$ distribution, we compute the area below both distributions. Similarity is defined as

$$S \equiv \int_0^\infty dx \, \min\{P_{diff}(x), P_{DMPK}(x)\}. \qquad [4]$$

By this definition S is bounded in [0, 1]. For additional information, see *Similarity Function $S(\nu, \chi)$*.

1. Joannopoulos JD, Johnson SG, Winn JN, Meade RD (2008) *Photonic Crystals: Molding the Flow of Light* (Princeton Univ Press, Princeton).
2. Benedek GB (1971) Theory of transparency of the eye. *Appl Opt* 10:459–473.
3. Rojas-Ochoa LF, Mendez-Alcaraz JM, Sáenz JJ, Schurtenberger P, Scheffold F (2004) Photonic properties of strongly correlated colloidal liquids. *Phys Rev Lett* 93:73903.
4. Reufer M, Rojas-Ochoa LF, Eiden S, Sáenz JJ, Scheffold F (2007) Transport of light in amorphous photonic materials. *Appl Phys Lett* 91:171904.
5. García PD, Sapienza R, Blanco Á, López C (2007) Photonic glass: A novel random material for light. *Adv Mater* 19:2597–2602.
6. Prum RO, Torres RH, Williamson S, Dyck J (1998) Coherent light scattering by blue feather barbs. *Nature* 396:28–29.
7. Ashcroft NW, Lekner J (1966) Structure and resistivity of liquid metals. *Phys Rev* 145:83–90.
8. Fraden S, Maret G (1990) Multiple light scattering from concentrated, interacting suspensions. *Phys Rev Lett* 65:512–515.
9. Conley GM, Burresi M, Pratesi F, Vynck K, Wiersma DS (2014) Light transport and localization in two-dimensional correlated disorder. *Phys Rev Lett* 112:143901.
10. Wiersma DS, van Albada MP, van Tiggelen BA, Lagendijk A (1995) Experimental evidence for recurrent multiple scattering events of light in disordered media. *Phys Rev Lett* 74:4193–4196.
11. Rezvani Naraghi R, Sukhov S, Sáenz JJ, Dogariu A (2015) Near-field effects in mesoscopic light transport. *Phys Rev Lett* 115:203903.
12. Florescu M, Torquato S, Steinhardt PJ (2009) Designer disordered materials with large, complete photonic band gaps. *Proc Natl Acad Sci USA* 106:20658–20663.
13. Froufe-Pérez LS, et al. (2016) Role of short-range order and hyperuniformity in the formation of band gaps in disordered photonic materials. *Phys Rev Lett* 117: 053902.
14. Abrahams E, Anderson PW, Licciardello DC, Ramakrishnan TV (1979) Scaling theory of localization: Absence of quantum diffusion in two dimensions. *Phys Rev Lett* 42: 673–676.
15. Markoš P (2006) Numerical analysis of the Anderson localization. *Acta Phys Slovaca Rev Tutorials* 56:561–685.
16. Yablonovitch E (1987) Inhibited spontaneous emission in solid-state physics and electronics. *Phys Rev Lett* 58:2059–2062.
17. John S (1987) Strong localization of photons in certain disordered dielectric superlattices. *Phys Rev Lett* 58:2486–2489.
18. Batten RD, Stillinger FH, Torquato S (2008) Classical disordered ground states: Superideal gases and stealth and equi-luminous materials. *J Appl Phys* 104:033504.
19. Leseur O, Pierrat R, Carminati R (2016) High-density hyperuniform materials can be transparent. *Optica* 3:763.
20. Edagawa K, Kanoko S, Notomi M (2008) Photonic amorphous diamond structure with a 3D photonic band gap. *Phys Rev Lett* 100:013901.
21. Liew SF, et al. (2011) Photonic band gaps in three-dimensional network structures with short-range order. *Phys Rev A* 84:063818.
22. Torquato S, Stillinger FH (2003) Local density fluctuations, hyperuniformity, and order metrics. *Phys Rev E* 68:041113.
23. Torquato S, Zhang G, Stillinger FH (2015) Ensemble theory for stealthy hyperuniform disordered ground states. *Phys Rev X* 5:21020.
24. John S (1996) Localization of light: Theory of photonic band gap materials. *Photonic Band Gap Materials* (Springer, Rotterdam), pp 563–665.
25. Scheffold F, Lenke R, Tweer R, Maret G (1999) Localization or classical diffusion of light? *Nature* 398:206–207.
26. Skipetrov SE, Page JH (2016) Red light for Anderson localization. *New J Phys* 18:021001.
27. Skipetrov SE, Sokolov IM (2014) Absence of Anderson localization of light in a random ensemble of point scatterers. *Phys Rev Lett* 112:023905.
28. Wiersma DS, Bartolini P, Lagendijk A, Righini R (1997) Localization of light in a disordered medium. *Nature* 390:671–673.
29. Schuurmans FJP, Vanmaekelbergh D, van de Lagemaat J, Lagendijk A (1999) Strongly photonic macroporous gallium phosphide networks. *Science* 284:141–143.
30. Deych LI, Lisyansky AA, Altshuler BL (2001) Single-parameter scaling in one-dimensional Anderson localization: Exact analytical solution. *Phys Rev B* 64:224202.
31. Prior J, Somoza AM, Ortuño M (2005) Conductance fluctuations and single-parameter scaling in two-dimensional disordered systems. *Phys Rev B* 72:024206.
32. Torres JA, Sáenz JJ (2004) Improved generalized scattering matrix method: Conduction through ballistic nanowires. *J Phys Soc Jpn* 73:2182–2193.
33. Beenakker CWJ (1997) Random-matrix theory of quantum transport. *Rev Mod Phys* 69:731–808.
34. Chabanov AA, Stoytchev M, Genack AZ (2000) Statistical signatures of photon localization. *Nature* 404:850–853.
35. Dorokhov ON (1982) Transmission coefficient and the localization length of an electron in N bound disordered chains. *ZhETF Pisma Redaktsiiu* 36:259.
36. Mello P, Pereyra P, Kumar N (1988) Macroscopic approach to multichannel disordered conductors. *Ann Phys* 181:290–317.
37. Froufe-Pérez LS, García-Mochales P, Serena PA, Mello PA, Sáenz JJ (2002) Conductance distributions in quasi-one-dimensional disordered wires. *Phys Rev Lett* 89:246403.
38. Muttalib KA, Wölfle P (1999) "One-sided" log-normal distribution of conductances for a disordered quantum wire. *Phys Rev Lett* 83:3013–3016.
39. Somoza AM, Prior J, Ortuño M, Lerner IV (2009) Crossover from diffusive to strongly localized regime in two-dimensional systems. *Phys Rev B* 80:212201.
40. Sellers SR, Man W, Sahba S, Florescu M (2017) Local self-uniformity in photonic networks. *Nat Commun* 8:14439.
41. John S (1984) Electromagnetic absorption in a disordered medium near a photon mobility edge. *Phys Rev Lett* 53:2169–2172.
42. Xie R, et al. (2013) Hyperuniformity in amorphous silicon based on the measurement of the infinite-wavelength limit of the structure factor. *Proc Natl Acad Sci USA* 110:13250–13254.
43. Izrailev F, Krokhin A, Makarov N (2012) Anomalous localization in low-dimensional systems with correlated disorder. *Phys Rep* 512:125–254.
44. Johnson S, Joannopoulos J (2001) Block-iterative frequency-domain methods for Maxwell's equations in a planewave basis. *Opt Express* 8:173–190.
45. Mello P, Yépez M, Froufe-Pérez L, Sáenz J (2006) Statistical scattering of waves in disordered waveguides: Universal properties. *Phys Stat Mech Appl* 372:203–209.
46. Froufe-Pérez LS, Carminati R, Sáenz JJ (2007) Fluorescence decay rate statistics of a single molecule in a disordered cluster of nanoparticles. *Phys Rev A* 76:013835.
47. Pichard J-L (1991) *Quantum Coherence in Mesoscopic Systems* (Plenum, New York).

5

Supporting Information

Froufe-Pérez et al. 10.1073/pnas.1705130114

Relations Between Degree of Stealthiness, Wave Numbers, and Frequencies

Stealthy hyperuniform structures are defined through their structure factor (18). There is a critical wave number k_c, below which the structure factor identically vanishes, $S(k < k_c) \equiv 0$. In this study, we work with structures where the scattering units are placed according to randomly generated SHU point patterns. In all cases, the finite size patterns have N points and are generated in a square where periodic boundary conditions are applied.

The parameter controlling the structural properties of the samples is the degree of stealthiness χ defined as the ratio of the constrained degrees of freedom (i.e., number of constrained wave numbers) to the total number of degrees of freedom. In a sample with $N \gg 1$ particles in two dimensions with periodic boundary conditions, the possible wave vectors $\mathbf{k}_{nm}$ compatible with periodic boundary conditions are discretized. In the particular case of a square cell of side L, we have

$$\mathbf{k}_{nm} = \frac{2\pi}{L} \begin{pmatrix} n \\ m \end{pmatrix} \qquad \text{[S1]}$$

with integers n, m. Hence, the number of constraints can be approximated by

$$\# \text{ constrained } \mathbf{k} \simeq \frac{\pi k_c^2}{(2\pi/L)^2} = \frac{(k_c L)^2}{4\pi}. \qquad \text{[S2]}$$

On the other hand, the total number of degrees of freedom for a system of N points is $\sim 2N$ in two dimensions. Hence, the degree of stealthiness is

$$\chi \simeq \frac{(k_c L)^2}{8\pi N}. \qquad \text{[S3]}$$

This approximation is exact in the limit of large particle number and large cell size at constant density.

We consider a length unit a such that the number density is $\rho = N/L^2 \equiv a^{-2}$. Using this definition, we can write $\chi = (k_c a)^2/8\pi$, or

$$k_c = \sqrt{\frac{8\pi\chi}{a^2}}. \qquad \text{[S4]}$$

We can associate features in the structure factor with spectral features. Throughout this work we consider transport and the DOS in TM polarization for collections of nonoverlapping rods. We keep the rod density (filling fraction) constant. Hence, the effective permittivity (and refractive index) $\epsilon_{\text{eff}} = n_{\text{eff}}^2$ of the sample is also a constant irrespective of χ, at least in the low-energy regime. Any spectral feature related to scattering at a given vacuum wavelength λ_0 can be related to a maximum scattering wave number in the effective medium,

$$k_f = 2\frac{2\pi}{\lambda_0} n_{\text{eff}}, \qquad \text{[S5]}$$

where we explicitly separate a factor 2 to stress that the momentum transfer is two times the wave momentum as in Bragg's law.

If the maximum scattering wavenumber in the effective medium $k_{\text{max}} = 4\pi n_{\text{eff}}/\lambda_0$ is smaller than the critical wave number k_c then single scattering in the medium is inhibited. This condition defines the stealth region. In terms of frequency ν and degree of stealthiness χ, the boundary of the stealth region is defined by

$$\chi(\nu) = 2\pi \left(\frac{\nu a}{c} n_{\text{eff}} \right)^2 \qquad \text{[S6]}$$

Above this value of χ the system is stealthy at the frequency ν.

Generation of Point Patterns and Band Structure Calculations

We use a simulated annealing relaxation scheme to generate disordered SHU patterns with $S(k) < 10^{-6}$ for $k < k_c(\chi)$, as described in our previous work (13). Patterns below the critical parameter $\chi \sim 0.55$, above which quasi-long-range order gradually appears (23), already show significant short-range order. The point patterns are decorated with dielectric cylinders as described in the main text.

NDOSs are calculated by using the supercell method (1) implemented in the open source code MIT Photonic Bands (44). The supercell is repeated periodically and the band structure is calculated by following the path $\Gamma \to M \to X \to \Gamma$ in reciprocal space. The procedure is described in detail in our prior work (13). Nearly identical strategies have also been applied by others (12).

Isotropy of the SHU Seed Patterns

Eventually, for high enough values of χ, entropic crystallization starts to emerge. We expect the optical properties of isotropic systems to deviate from the ones of nonisotropic structures. By generating 1000 independent samples for each considered value of χ, we determine the degree of isotropy by analyzing the angular distribution of $S(\mathbf{k})$. We use the same sampling as the one used for transport and DOS calculations. In particular, we compute angular fluctuations of the 2D structure factor $S(\mathbf{k})$ for each of the samples. If a given sample presents angular fluctuations above a given threshold, it is considered as nonisotropic. We define the isotropy as the ratio of the samples with angular fluctuations below the threshold to total the number of samples. We set the anisotropy threshold to the maximum angular fluctuation of the structural sampling for $\chi = 0.10$ plus a 0.1% margin. In this way, by definition, all samples for $\chi = 0.10$ are isotropic.

We find that nearly all considered samples are isotropic for $\chi \leq 0.45$; nearly all samples show strong anisotropy for $\chi \geq 0.55$; and for $\chi = 0.50$, $\sim 70\%$ of the samples are isotropic. Fig. S1 shows the results of the isotropy calculations together with some representative examples of the patterns in real space and (zoomed) maps of the structure factor $S(\mathbf{k})$. There is a clear distinction between samples showing small variations and those showing large variation of the angular distribution of the structure factor. In the former case, large angular fluctuations are followed by the emergence of a sixfold pattern signaling sample crystallization.

GSM Method

We describe the GSM method used in the transport calculations (32). Throughout this work, TM polarization has been used. In this case, the electric fields are parallel to the axis of the cylindrical scattering units (axis along $\mathbf{u}_z$ direction). The electric field is hence equivalent to a scalar field, which, in the frequency domain, can be written as

$$\mathbf{E}(\mathbf{r}, \omega) = E(x, y, \omega)\mathbf{u}_z, \qquad \text{[S7]}$$

where we explicitly state the x, y dependence of the scalar field E. The wave equation with this geometry reduces to the scalar wave equation

$$\nabla^2 E + \left(\frac{\omega}{c}\right)^2 \epsilon(x,y) E = 0 \qquad \textbf{[S8]}$$

in the absence of sources. We assume a dependence of E on the coordinates x, y and frequency ω. Throughout this work, the permitivity ϵ is assumed to be independent of the frequency. The field-matching conditions for the scalar electric field E across any discontinuity of the permittivity are continuity of E and its first derivatives $\partial_x E$ and $\partial_y E$.

All structures considered in this work have been generated in a square cell of size $L_{\max} \times L_{\max}$ using periodic boundary conditions. To avoid spurious effects in the evaluation of light transport properties, we use the same periodic boundary conditions in solving the wave equation. We choose one of the directions parallel to one edge of the simulation cell to be the transport direction x. y is the transverse direction. We discretize the spatial domain in slices of thickness Δx in the transport direction. If the slices are chosen sufficiently thin, then we can approximate the permittivity $\epsilon(x,y)$ as being independent of x within the slice. We furthermore discretize the permittivity spatial profile in the transverse direction using a step $\Delta y = \Delta x$. In this way, we avoid introducing spurious anisotropy due to the shape of the elemental building blocks. In Fig. S2, we show an example of the discretization procedure on a sample. In particular, we notice that in the pixelization procedure, an antialiasing procedure is followed to ensure that the filling fraction of the system in the GSM method is kept at its correct value even after discretization. We use a 5×5 supersampling scheme for antialiasing.

In any given slice perpendicular to x, the permittivity is independent on x. Hence, assuming periodic boundary conditions, the electric field at the i-th slice can be written as a superposition of modes,

$$E^{(i)} = \sum_{n=1}^{\infty} \phi_n^{(i)}(y) \left[A_n^{(i)} \frac{e^{ik_{x,n}^{(i)}(x-x_i)}}{|k_{x,n}^{(i)}|^{1/2}} + B_n^{(i)} \frac{e^{-ik_{x,n}^{(i)}(x-x_i)}}{|k_{x,n}^{(i)}|^{1/2}} \right].$$
$$\textbf{[S9]}$$

We are assuming that the i-th slice spans in $x \in [x_i - \Delta x/2, x_i + \Delta x/2]$, and the solution is valid only in this interval. The additional dephasing induced by the terms x_i is introduced to enhance numerical stability, in particular when the wavenumbers $k_{x,n}^{(i)}$ are purely imaginary (exponential growth away from interfaces). Also, the denominators $|k_{x,n}^{(i)}|^{1/2}$ are included to normalize modes to unitary intensity in the propagation direction if the mode profile $\phi_n^{(i)}$ is properly normalized.

The transverse modes $\phi_n^{(i)}$ are solutions of the eigenvalue equation

$$\partial_{yy} \phi_n^{(i)}(y) + \left(\frac{\omega}{c}\right)^2 \epsilon^{(i)}(y) \phi_n^{(i)}(y) = \left(k_{x,n}^{(i)}\right)^2 \phi_n^{(i)}(y). \quad \textbf{[S10]}$$

They satisfy periodic boundary conditions. The function $\epsilon^{(i)}(y)$ is the permittivity restricted to the i-th slice and only depends on y. At this point, the Bloch theorem can be invoked to obtain solutions. In our calculations, we take the Bloch wave vector to be $\mathbf{0}$ (Gamma point). By doing so, the solutions are also purely periodic in the transverse direction, and the modes can be written as a superposition of plane waves in the form

$$\phi_n^{(i)}(y) = \sum_{m=-\infty}^{\infty} e^{i\frac{2\pi m}{L_{\max}}y} \phi_{m,n}^{(i)}. \qquad \textbf{[S11]}$$

With this, we can recast Eq. **S10** in algebraic form,

$$M \vec{\phi}_n = (k_{x,n})^2 \vec{\phi}_n, \qquad \textbf{[S12]}$$

where the vector $\vec{\phi}_n^{(i)}$ is defined through $\left(\vec{\phi}_n^{(i)}\right)_m \equiv \phi_{m,n}^{(i)}$. The $M^{(i)}$ matrix elements are

$$M_{mn}^{(i)} = -\delta_{mn} \left(\frac{2\pi n}{L_{\max}}\right)^2 + \left(\frac{\omega}{c}\right)^2 \epsilon_{m,n}^{(i)}, \qquad \textbf{[S13]}$$

where

$$\epsilon_{m,n}^{(i)} \equiv \frac{1}{L_{\max}} \int_0^{L_{\max}} \epsilon^{(i)}(y) e^{2\pi i(n-m)\frac{y}{L_{\max}}}. \qquad \textbf{[S14]}$$

After introducing a high-frequency cutoff, we end up with a finite matrix $M^{(i)}$ in the eigenvalue problem given by Eq. **S12** that is now suitable for numerical evaluation. Considering the expressions Eqs. **S13** and **S14**, the matrix M is explicitly Hermitian; hence, its eigenvalues $\left(k_{x,n}^{(i)}\right)^2$ are real, but not necessarily positive. The corresponding eigenmodes are denoted as $|n^{(i)}\rangle$ in bra-ket notation and are normalized to $\langle m^{(i)}|n^{(i)}\rangle = \delta_{nm}$. The dimensions of the matrix $M^{(i)}$ have to be chosen in such a way that enough evanescent modes, $\left(k_{x,n}^{(i)}\right)^2 < 0$, are considered.

Once we have a complete description of the fields in the i-th slice, we have to couple them to adjacent ones. To do so, first we consider that we can couple a single slice at both sides to vacuum, and we obtain the scattering matrix of this isolated system including evanescent modes. The vacuum is considered to be media $(i-1)$ and $(i+1)$. The scattering matrix $s^{(i)}$ relates the incoming and outgoing vacuum amplitudes,

$$\begin{pmatrix} \mathbf{B}^{(i-1)} \\ \mathbf{A}^{(i+1)} \end{pmatrix} = s^{(i)} \begin{pmatrix} \mathbf{A}^{(i-1)} \\ \mathbf{B}^{(i+1)} \end{pmatrix} \equiv \begin{bmatrix} r^{(i)} & \tilde{t}^{(i)} \\ t^{(i)} & \tilde{r}^{(i)} \end{bmatrix} \begin{pmatrix} \mathbf{A}^{(i-1)} \\ \mathbf{B}^{(i+1)} \end{pmatrix}. \quad \textbf{[S15]}$$

The specific values of the transmission matrices ($t^{(i)}$ and $\tilde{t}^{(i)}$) and reflection matrices ($r^{(i)}$ and $\tilde{r}^{(i)}$) are found by imposing C^1 continuity at the boundaries of the slice.

To obtain the scattering matrix of a set of two adjacent slices (i and $i+1$) surrounded by vacuum, we combine the corresponding scattering matrices $s^{(i)}$ and $s^{(i+1)}$ to

$$s^{(i)} \circ s^{(i+1)} \equiv s \equiv \begin{bmatrix} r & \tilde{t} \\ t & \tilde{r} \end{bmatrix}, \qquad \textbf{[S16]}$$

where

$$r = r^{(i)} + \tilde{t}^{(i)} r^{(i+1)} Q t^{(i)} \qquad \textbf{[S17a]}$$

$$t = t^{(i+1)} Q t^{(i)} \qquad \textbf{[S17b]}$$

$$\tilde{t} = \tilde{t}^{(i)} \tilde{t}^{(i+1)} + \tilde{t}^{(i)} r^{(i+1)} Q \tilde{r}^{(i)} \tilde{t}^{(i+1)} \qquad \textbf{[S17c]}$$

$$\tilde{r} = \tilde{r}^{(i+1)} + t^{(i+1)} Q \tilde{r}^{(i)} \tilde{t}^{(i+1)} \qquad \textbf{[S17d]}$$

$$Q \equiv \left[\mathbb{I} - \tilde{r}^{(i)} r^{(i+1)} \right]^{-1}. \qquad \textbf{[S17e]}$$

The identity matrix $\mathbb{I}$ has dimension $N_{\text{vac}} \times N_{\text{vac}}$ with the number of modes in vacuum including evanescent modes N_{vac}.

In the calculation of the total scattering matrix of the system, we calculate the scattering matrix of each slice and then accumulate the total scattering by recursively applying the formulas **[S17]**. We set $s^{(i)}$ to the accumulated matrix and $s^{(i+1)}$ to the scattering matrix corresponding to the new slice attached to the system. Once we obtained the total scattering matrix, channel–channel transmittances $T_{ab} \equiv |t_{ab}|^2$, total transmittances $T_a \equiv \sum_b T_{ba}$, and conductance $g \equiv \sum_a T_a$ is calculated by varying the indexes a and b only through the propagating modes corresponding to asymptotic scattering states.

One of the advantages of this method is that the accumulated scattering matrix at intermediate steps provides transport information for all accumulated lengths of the system (i.e., all of the way from $L = 0$ to $L = L_{\max}$). Fig. S3A shows the average over 1,000 samples of $\ln(g)$ for several frequencies at

$\chi = 0.35$ and a system of $N \simeq 196$ particles. To obtain the decay length ξ, $\langle \ln(g) \rangle$ is fitted to a straight line for lengths such that $\langle \ln(g) \rangle \leq \ln 1/2 \simeq -0.7$. This threshold value corresponds to the dashed line in the figure. Fig. S3*B* sketches the procedure followed in the GSM method. The scattering matrix of each system is calculated for lengths $L \leq L_{max}$, increasing the length pixel by pixel. In all numerical calculations, we considered 500×500 pixels.

DMPK Equation

The DMPK equation (35, 36) is a Fokker–Planck equation describing the evolution of coherent wave transport statistics as a function of the ratio of the system length to the transport mean free path. It is a suitable description for disordered Q1D systems.

We consider a Q1D system of length L supporting a given number of propagating channels N. The corresponding asymptotic scattering matrix S of the system with dimension $2N \times 2N$ can be explicitly written in terms of the transmission (t and $\tilde{t}$) and reflection (r and $\tilde{r}$) matrices as in Eq. **S15**. By using the singular value decomposition of each of the scattering matrix entries, the scattering matrix can be expressed in terms of the polar decomposition

$$S = \begin{bmatrix} r & \tilde{t} \\ t & \tilde{r} \end{bmatrix} = \begin{bmatrix} u & 0 \\ 0 & v \end{bmatrix} \begin{bmatrix} -\sqrt{1-\tau} & \sqrt{\tau} \\ \sqrt{\tau} & \sqrt{1-\tau} \end{bmatrix} \begin{bmatrix} u^t & 0 \\ 0 & v^t \end{bmatrix},$$

[S18]

where the $N \times N$ matrices u and v are unitary. The matrix of singular values $\tau = \text{diag}\{\tau_i\}$, $i = 1, \ldots, N$ is given by the transport eigenvalues $\{\tau_i\}$. This specific form of the scattering matrix holds only for systems where reciprocity is preserved (the so-called $\beta = 1$ universality class).

All statistical scattering magnitudes can be derived from the statistical distribution of the scattering matrix $P_L(S)$ for a system of a given length L. The DMPK equation provides such a distribution based on a few simplifying assumptions.

We consider that the transport eigenvalues (radial variables) and the unitary matrices (angular variables) are statistically independent. We further assume that the unitary matrices u and v are distributed according to the unitary group (i.e., according to the Haar measure). This approach is known as the isotropy hypothesis. Within this approach, it is obvious that the distribution of angular variables is independent of the length of the system L and that all evolution of the statistical transport with L is given by the evolution of the joint probability distribution of the transport eigenvalues $P_L(\{\tau_i\})$.

We further assume that the scattering matrix s corresponding to a slice of disordered material attached to the system of length L is statistically independent of the previous $P_L(S)$ both for the angular variables (u and v) and for the transport eigenvalues $\{\tau_i\}$.

The last assumption introduces a scaling length ℓ that can be interpreted as the transport mean free path. It is assumed that there exist a length ℓ such that the averaged conductance $\langle g \rangle_{\delta L}$ of a disordered region of length δL is $\langle g \rangle_{\delta L} = N(1 - \delta L/\ell)$. If the transport eigenvalues of the corresponding scattering matrix are $\{\delta_i\}$, it is considered that higher-order moments of the conductance scales at least as the same order of $\delta L/\ell$.

With all these assumptions, applying **[S16]** to compute the scattering matrix $S_{L+\delta L}$ resulting from the composition of the scattering matrices S_L and $S_{\delta L}$, the change in the joint probability distribution (JPD) function of the transport eigenvalues can be found, the so-called DMPK equation,

$$\frac{\partial P(\{x_i\}, s)}{\partial s} = \frac{1}{2\gamma} \sum_{n=1}^{N} \frac{\partial}{\partial x_n} \left[\frac{\partial P}{\partial x_n} + P \frac{\partial \Omega}{\partial x_n} \right], \quad \textbf{[S19]}$$

where we have performed the variable changes $\cosh^2(x_n) \equiv 1/\tau_n$, $s \equiv L/\ell$ and defined $\gamma \equiv N + 1$. The interaction term $\Omega(\{x_i\})$ is

$$\Omega = -\sum_{i=1}^{N-1} \sum_{j=i+1}^{N} \ln |\sinh^2(x_j) - \sinh^2(x_i)| - \sum_{i=1}^{N} \ln |\sinh(2x_i)|.$$

[S20]

Unfortunately, there is no known analytical solution to Eq. **S20**. An approximate solution for the JPD of $\{x_i\}$ is (33)

$$P(\{x_i\}, s) \propto \prod_{i<j} |\sinh^2(x_j) - \sinh^2(x_i)|^{\frac{1}{2}} |x_j^2 - x_i^2|^{\frac{1}{2}}$$
$$\times \prod_{i=1}^{N} e^{-x_i^2 \frac{\gamma}{2s}} (x_i \sinh(2x_i))^{\frac{1}{2}}. \quad \textbf{[S21]}$$

This approximation has been tested numerically against microscopic models and Monte Carlo (MC) simulations of the DMPK equation. Due to the isotropy hypothesis, the description of the statistical transport breaks down in the quasiballistic regime, where $L < \ell$. However, in the diffusive and localized regimes, $L \gg \ell$, the approximation **[S21]** gives excellent results compared with microscopic statistical simulations. In particular, the conductance distribution that can be obtained from MC simulation of this JPD function is indistinguishable from the ones obtained from full wave simulations or by using more sophisticated statistical transport theories (37, 45) in the diffusive and localized regimes.

The DMPK conductance distribution at a fixed average $\langle g \rangle = 1/2$ has been considered as a representative case in the crossover to Anderson localization in the SPS regime. The $P(g)$ used in this work were obtained via different sampling techniques (as explained below) applied to the JPD function **[S21]**.

Fig. S4 illustrates the results obtained after MC sampling of the JPD function **[S21]**. As can be seen, for $N = 5$ propagating channels, the statistical noise in the conductance distribution is negligible after 10^7 MC single channel steps. Nevertheless, for 10^3 MC single channel steps, the statistical noise due to finite sampling is large. If a limit of 10^3 is imposed in the sampling, a much larger bin size for the histogram has to be used to reduce noise. This is the case in below, where we compare the GSM method and DMPK conductance distributions obtained after a sampling of size 1000.

Similarity Function S(ν, χ)

The quantitative evaluation of the similarity between conductance distributions of the correlated systems and those of DMPK are limited by finite sampling artifacts of the DMPK conductance histograms. We quantify the differences by calculating a squared distance distribution function $P(D^2)$. The squared distance between two distributions $P_i(g)$ and $P_j(g)$ is given by

$$D_{i,j}^2 \equiv \int dg \, [P_i(g) - P_j(g)]^2. \quad \textbf{[S22]}$$

In other contexts, the squared distance D^2 is denoted χ^2 or chi-squared. We do not make use of this notation to avoid confusion with the degree of stealthiness χ. For a set of different, but otherwise statistically equivalent, finite-sampling distributions $P_i(g)$, we can define the distribution of squared distances $P(D^2)$ considering all distances $D_{i,j}$ corresponding to all pairs with $i \neq j$.

We further assume that any histogram showing the same D^2 distribution with the previous members or the DMPK distributions is a qualified member of the ensemble. To build an appropriate $P(D^2)$ distribution, we performed a conductance sampling using the DMPK model mimicking the way the GSM method conductance distributions at $\langle g \rangle = 1/2$ are obtained: We take a system length such that $\langle g \rangle \simeq 1/2$ for 1,000 independent

samples. In this way, we perform an MC sampling while scanning the system length within a certain range. For each sampling, we choose the length associated to the value of the averaged conductance closest to 1/2. A key point is using equivalent sampling. In the DMPK case, we also take 1,000 independent samples. We repeat the procedure to generate $N = 1000$ independent histograms with $\langle g \rangle \simeq 1/2$. We consider each DMPK histogram as a qualified member of the ensemble of conductance histograms build with 1,000 samples and fixed bin size. All DMPK pairs of histograms define a D^2 distribution function $P_{\text{DMPK}}(D^2)$. This distribution function is shown as black histograms in Fig. S5 *D–F*.

We furthermore assume that any particular conductance histogram should show the same D^2 distribution compared with each of the members of the DMPK sampling. In other words, the distribution $P_{\text{diff}}(D^2)$ created with all of the $D^2_{\text{diff},i}$, $i = 1, \ldots, N$ (N being the number of independent DMPK histograms) defined through

$$D^2_{\text{diff},i} \equiv \int dg \, [P_{\text{GSM}}(g) - P_i(g)]^2, \qquad \text{[S23]}$$

where $P_{\text{GSM}}(g)$ is the single conductance distribution we compare against the DMPK model, should be $P_{\text{diff}}(D^2) = P_{\text{DMPK}}(D^2)$.

To assess the similarity between $P_{\text{diff}}(D^2)$ and the reference $P_{\text{DMPK}}(D^2)$ distribution, we compute the area below both distributions. Similarity is defined as

$$S(\nu, \chi) \equiv \int_0^\infty dx \, \min\{P_{\text{diff}}(x), P_{\text{DMPK}}(x)\}. \qquad \text{[S24]}$$

By this definition, $S(\nu, \chi)$ is bounded in $[0, 1]$.

We regard the overlapping integral (gray shaded area in Fig. S5 *D–F* as the probability of a given GSM method conductance histogram to belong to the DMPK ensemble. In fact, this procedure gives a good quantitative measure of the similarity that can be guessed by mere inspection. The red histograms in Fig. S5 *D–F* are the GSM-DMPK D^2 distributions calculated for the corresponding systems shown in Fig. S5 *D–F, Right*. In Fig. S5*D*, the similarity is $S(\nu, \chi) \simeq 0.89$, and, as stated above, the GSM method conductance distribution (red histogram, Fig. S5*A*) looks highly similar to the converged DMPK one (black distribution in Fig. S5 *A–C*). This last distribution is built out of 10^8 independent samples. In Fig. S5*B*, we have a less similar GSM conductance distribution, although still resembling the main features of the DMPK one. In this case, $S \simeq 0.50$. Finally, in Fig. S5*F*, we have a null overlap between GSM and DMPK D^2 distributions; hence, $S = 0$ and, as can be seen in the corresponding left panel, DMPK and GSM conductance distributions are highly dissimilar for this particular value of $\chi = 0.45$. This fact indicates that the underlying transport mechanisms are different from the ones assumed in the DMPK model.

This procedure for assessing the similarity of a particular GSM conductance distribution to the DMPK model is particularly sensitive to subtle variations in the parameters controlling the sampling and histogramming procedures. To compare both GSM and DMPK ensembles, sampling and histogramming have to be performed following the same procedure. For instance, comparing histograms with the same bin size but different number of samples gives rise to different results, even if the shape of the distribution is similar.

In all cases, the DMPK model results have been calculated by using an MC method using $N_{\text{prop}} = 5$ propagating channels. With this number of channels, the conductance distributions at $\langle g \rangle = 1/2$ are already converged to the same distribution found for $N_{\text{prop}} \gg 1$.

DOS

We have calculated the DOS as a function of the stealthiness parameter for systems of four different sizes ranging from

$N_p \simeq 100$ to $N_p \simeq 480$, where N_p is the number of rods in the structure. The exact number of rods in a pattern depends on the chosen values of χ. In Fig. S6, we show the raw DOS normalized to the number of rods in the structure. The raw DOS is a histogram of eigen-frequencies computed at 13 different points in the reciprocal space, each box of the histogram is then divided by the number of k-points, the number of disorder realizations, and the number of rods in each pattern. For a given value of χ, the number of rods is the same for all realizations of disorder. For $N_p \simeq 100, 200$ and $N_p \simeq 320$, we calculated the band structure of 500 independent disorder realizations, while for $N_p \simeq 480$ rods we have between 30 and 60 disorder realizations. As can be seen in Fig. S6, the DOS is independent on the size of the structure.

Local DOS. Finite size effects are expected in related quantities like the local DOS (LDOS), $LDOS(\mathbf{r}_e)$, proportional to the spontaneous emission rate of a point emitter located at $\mathbf{r}_e$. As predicted by Yablonovitch (16), the LDOS is expected to vanish at any point in a photonic crystal presenting a full PBG. While this holds for infinite systems, in finite samples there should also be a finite evanescent coupling to the modes in the continuum. Hence, the LDOS should decay exponentially to zero as the system size increases (provided the LDOS is calculated at a point close to the center of the material). We calculate the decay rate of an emitter placed in the center of the sample using a coupled dipole method described in detail elsewhere (46). In Fig. S7*A*, we plot the $LDOS(\mathbf{r}_e)$, normalized to vacuum's $LDOS$ ($LDOS_0$) for a single sample with $\chi = 0.40$ for different system sizes as shown in Fig. S7 *A, Inset* (N is the total number of scatterers). Fig. S7 shows the expected nearly exponential decay of the normalized $LDOS$ for a frequency $\nu a/c = 0.35$ inside the gap region, as a function of the system radius R/a (with $N = \pi(R/a)^2$). For system sizes as small as $N = 40$, the $LDOS$ is already three orders of magnitude smaller than $LDOS_0$.

Transport Characteristics

We perform identical statistical analysis on the $\ln(g)$ fluctuations as described in the main text also for systems of different sizes, $L_{\max} \simeq 10a$ ($N \simeq 100$ rods), $L_{\max} \simeq 18a$ ($N \simeq 310$ rods), and $L_{\max} \simeq 22a$ ($N \simeq 480$ rods). We find a similar behavior irrespective of system size. This result is summarized in Fig. S8. Therein, color maps of the $\ln(g)$ fluctuations at $L = L_{\max}$ (maximum size and square system) is plotted as a function of χ and $\nu a/c$ (Fig. S8 *A–C*). In Fig. S8 *D–F*, the corresponding color maps of a/ξ are also presented. As we can see, despite some differences in the values reached by the a/ξ and the $\ln(g)$ fluctuations, which are expected to grow with system size, the behavior as a function of χ and frequency does not depend on system size. In particular, the point of highest $\text{Var}(\ln(g))$ is found at a normalized frequency $\nu a/c \simeq 0.40$ and $\chi = 0.35$ in all cases. Table S1 summarizes the results found at this particular value of frequency and degree of stealthiness. We find a weak dependence of the decay length ξ as a function of system size. The prediction of the DMPK model for the localization length is $\xi_{\text{loc}} \propto (N_{\text{ch}} + 1)$, where N_{ch} stands for the number of propagating modes in the Q1D geometry. In the fourth and fifth columns of Table S1, we see that this is not the case at these particular values of χ and $\nu a/c$. On the contrary, the decay length shows a weak variation between $\xi/a \simeq 1.4$ and $\xi/a \simeq 1.7$ of the order of a factor 1.2, while the prediction for Q1D systems is a factor 2.25. On the other hand, the ratio $\text{Var}(\ln(g))/|\langle \ln(g) \rangle|$ roughly varies between 1.2 and 1.3— far from the predicted value of 2 for the Q1D geometries and close to the value of 1 found in ref. 47 and surprisingly similar to the value 1.24 found in ref. 15 using different models of strongly localized electronic 2D systems.
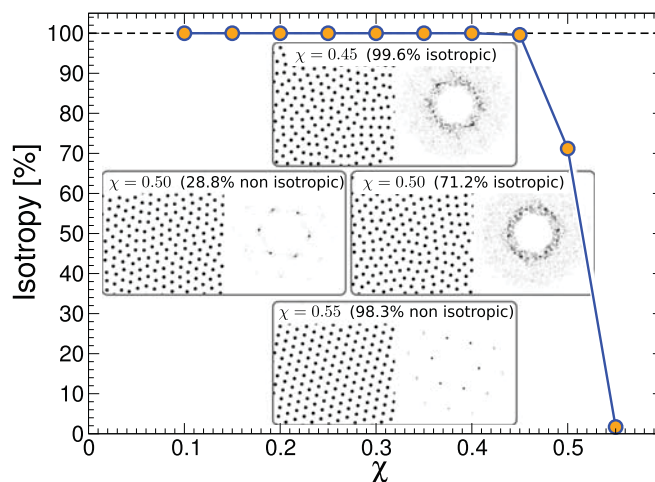
Fig. S1. Isotropy vs. χ. Each *Inset* shows an example of the patterns (*Left*) and corresponding structure factor (*Right*).
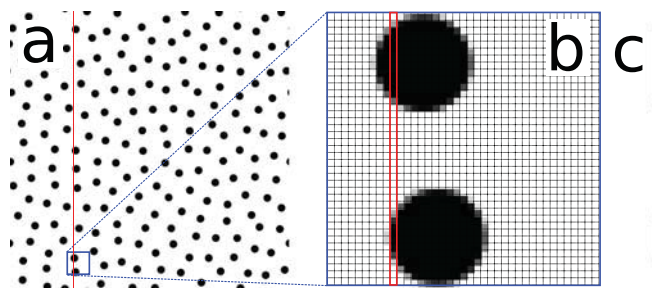
Fig. S2. (*A*) A 500 × 500 pixel image as considered by the GSM method. The distribution of rods corresponds to a single sample of a SHU distribution with $\chi = 0.40$. The rod radius is $r/a = 0.189$. There are $N \simeq 200$ rods in the periodic square cell. (*B*) Zoomed area of 40 × 40 pixels together with the grid corresponding to the pixelization. The effect of antialiasing is noticeable. (*C*) Part of a single stripe. The scattering matrix for each such stripe is calculated and then combined.
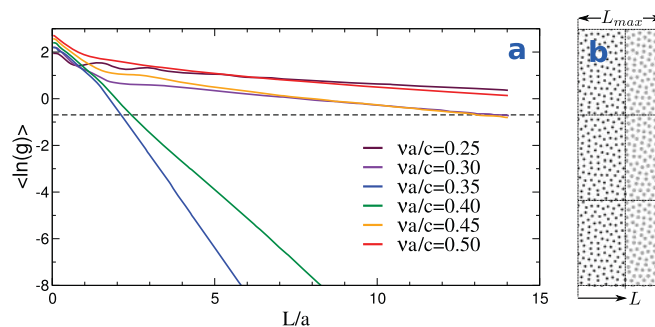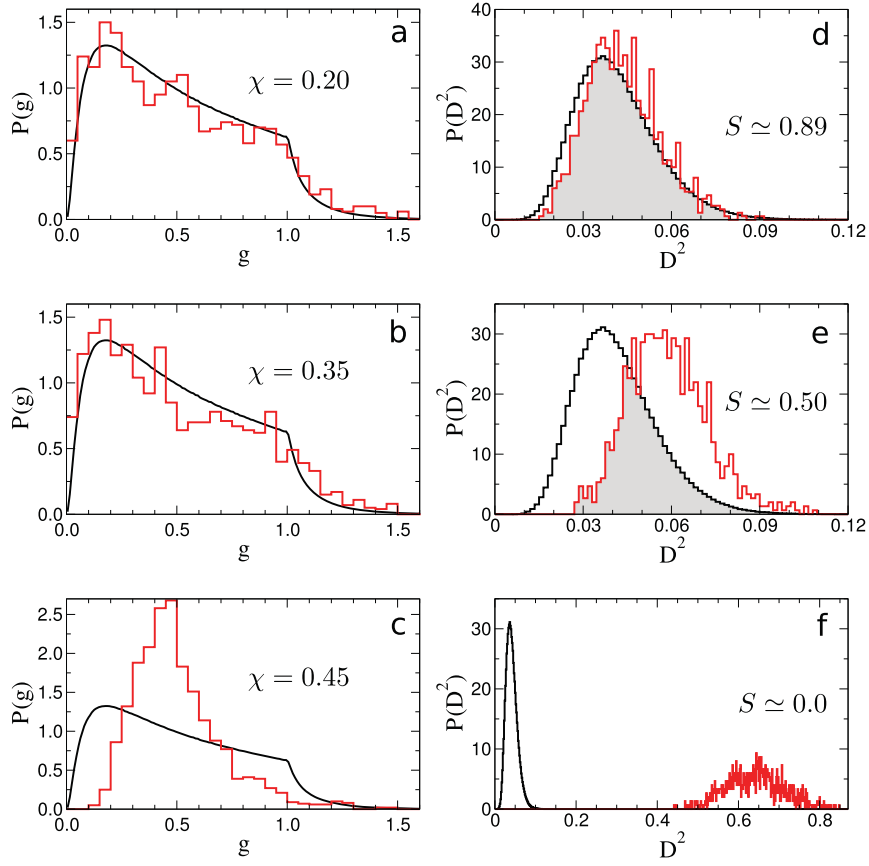

Fig. S3. (*A*) $\langle \ln(g) \rangle$ vs. L/a for a few selected frequencies (key) at $\chi = 0.35$. Averages taken over 1,000 independent samples. (*B*) Sketch of a sample studied.

10
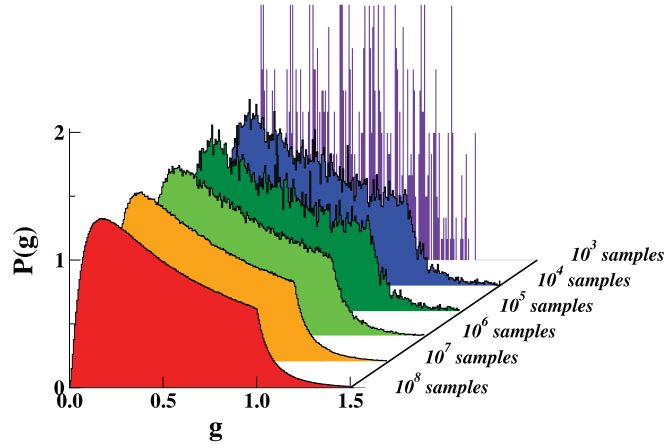
Fig. S4. Evolution of the conductance distribution with the number of MC steps (samples) for $N = 5$ for a converged value $\langle g \rangle = 1/2$. The MC calculation is performed by using the JPD function [S21].

Fig. S5. (*A–C*) Conductance distributions at $\langle g \rangle \simeq 1/2$ for different systems (red histograms) compared with the DMPK distribution obtained with 10^8 samples (black lines). All systems are calculated at $\nu a/c = 0.43$ and with different χ values (labeled). (*D–F*) The corresponding D^2 distributions (red) together with the D^2 distributions for the DMPK model (black). The overlap region (see text) is shaded in gray and represents the similarity $S(\nu, \chi)$. Similarities range from $S(\nu, \chi) = 0$ for $\chi = 0.45$ to $S(\nu, \chi) \simeq 0.89$ for $\chi = 0.20$.
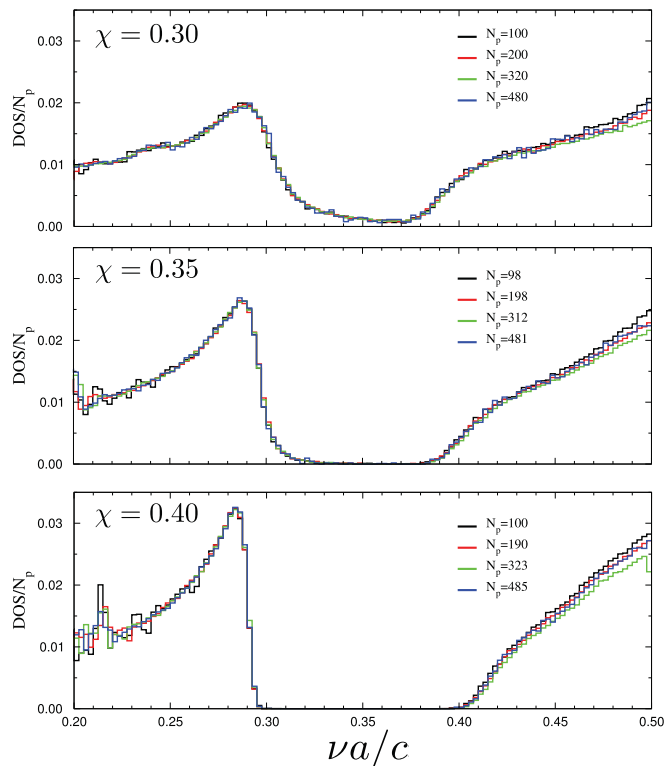
11

Fig. S6. DOS normalized by the number of rods (see text) for different sizes and stealthiness parameters in the region $\chi \in [0.3, 0.4]$ where the PBG opens.
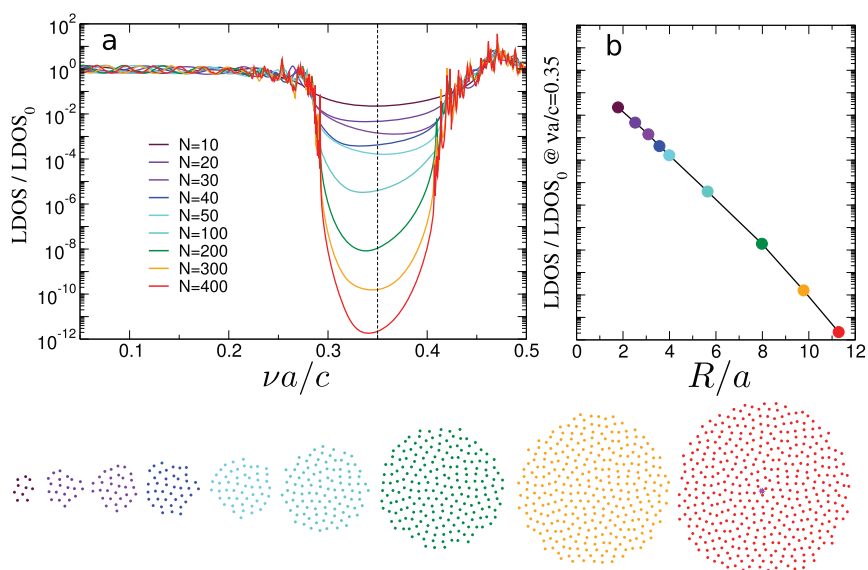

Fig. S7. (*A*) Local DOS, *LDOS*($\mathbf{r}_e$), normalized to vacuum's *LDOS* (*LDOS*$_0$) for a single finite sample with $\chi = 0.40$ as a function of the frequency ν for different system sizes (total number of particles *N*). The actual samples investigated are shown at the bottom and the central magenta colored point corresponds to $\mathbf{r}_e$. (*B*) Normalized *LDOS* for a frequency $\nu a/c = 0.35$ inside the gap region, as a function of the system radius *R/a* (with $N = \pi (R/a)^2$).

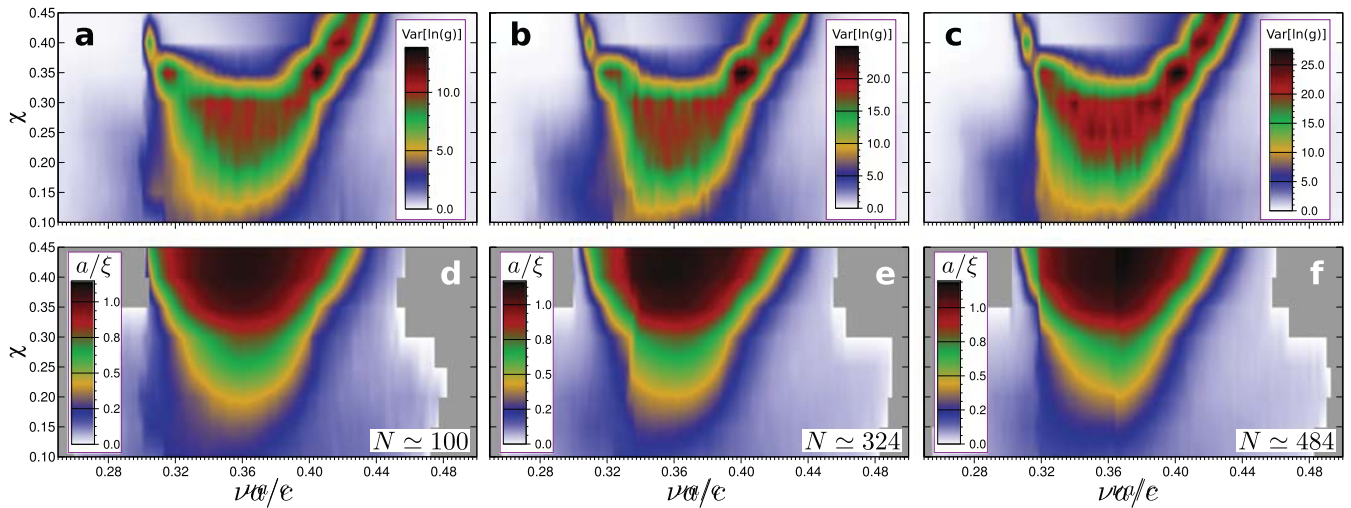**Fig. S8.** Color maps of Var(ln(g)) (A–C) and the inverse decay length a/ξ (D–F) as a function of χ and $\nu a/c$ for systems of different sizes. The number of scatterers in the simulation cell is indicated in each case. (D–F) The inverse decay length a/ξ is only weakly dependent on the system size.

Table S1. Number of propagating channels N_{ch}, size L_{max}/a, decay length ξ/a, ratio $\xi/[a(N_{ch}+1)]$, Var(ln(g)), $|\langle \ln(g)\rangle|$ and their ratio as a function of the number of cylinders in the patterns for $\chi = 0.35$ and normalized frequency $\nu a/c = 0.40$

N_{part}	L_{max}/a	N_{ch}	ξ/a	$\frac{\xi/a}{(N_{ch}+1)}$	Var $(\ln(g))$	$\|\langle\ln(g)\rangle\|$	$\frac{\text{Var}[\ln(g)]}{\|\langle\ln(g)\rangle\|}$
98	9.90	7	1.41	0.20	14.6	11.7	1.24
198	14.07	11	1.67	0.14	19.2	15.7	1.22
312	17.66	15	1.67	0.11	25.0	18.8	1.32
481	21.93	17	1.68	0.10	27.7	23.3	1.19